Surface & Coatings Technology 472 (2023) 129936

Contents lists available at ScienceDirect

Surface & Coatings Technology

journal homepage: www.elsevier.com/locate/surfcoat

Deposition of TiOx and N-TiOx by dielectric barrier discharge at atmospheric pressure

Adrien Chauvin [a,b,*], Carla Bittencourt [b], Mathilde Galais [c], Lionel Sauvage [d], Maxime Bellefroid [c], Carine Van Lint [c], Anne Op de Beeck [d], Rony Snyders [b,e], François Reniers [a]

[a] Chemistry of Surfaces, Interfaces and Nanomaterials, cp 255, Faculty of Sciences, Université libre de Bruxelles, 50 Avenue F.D. Roosevelt, 1050 Brussels, Belgium
[b] Plasma-Surface Interaction Chemistry, University of Mons, 23 Place du Parc, 7000 Mons, Belgium
[c] Service of Molecular Virology, Department of Molecular Biology (DBM), Université Libre de Bruxelles (ULB), Gosselies 6041, Belgium
[d] Center for Diabetes Research, Universite Libre de Bruxelles, 808 Route de Lennik, CP618, Brussels B-1070, Belgium
[e] Materia Nova Research Center, 3 Avenue Nicolas Copernic, 7000 Mons, Belgium

ARTICLE INFO

Keywords:
AP-DBD
TiOx
Thin-film
Nitrogen doping
Bandgap

ABSTRACT

Over the past years, atmospheric pressure deposition assisted by plasma has attracted interest due to its low cost. Among other materials deposited by this technology, titanium dioxide (TiO_2) is very popular, mostly due to its good photocatalytic properties. However, due to intrinsic drawbacks of the process, the control of the deposition parameters needs to be fine-tuned to obtain a thin film presenting the expected properties. Here we report the deposition of TiO_x and N-doped TiO_x thin films by dielectric barrier discharge at atmospheric pressure (AP-DBD) plasma with titanium (IV) isopropoxide and oxygen as reactants, and argon as a working gas during 10 min. In the first part, we highlight the advantages of heating the substrate at 400 °C during the deposition. Then, the influence of the oxygen content and power on the morphology and composition is reported. In the second part, we demonstrate the successful doping of the structure with nitrogen by adding ammonia (NH_3) to the working gas. Through a screening over deposition parameters (i.e. oxygen content and power), the lowest bandgap reachable was 3.22 eV for a working gas composed of 1.8 vol% of NH_3, 5, and 10 vol% of O_2, and a power of 75 W during the film deposition. Evaluating the formation of oxygen vacancies in the TiO_x films and the N doping, we were able to tentatively explain the observed evolution of the bandgap.

1. Introduction

In the past century, titanium dioxide (TiO_2) has been one of the most studied materials mainly due to its chemical stability, and its optical and photocatalytic properties in thin film form, which make it appealing for a large variety of applications such as sustainable energy generation or removal of environmental pollutants [1,2].

A wide range of techniques is now available to adapt the properties of TiO_2 thin films for the desired application, such as chemical vapor deposition (CVD) [3], sol-gel [4], inductive coupling plasma enhanced chemical deposition (ICP-PECVD) [5–7], and magnetron sputtering [8]. Although these methods have their advantages, they suffer from drawbacks, wet chemistry involves the generation of wastes, while relatively high-energy consumption is required for dry methods. Moreover, low-pressure approaches lead to high energy costs due to pumping. Among the different deposition techniques, Atmospheric Pressure Plasma (APP) has attracted interest for TiO_2 deposition due to its low cost, ease of scaling up, and, possibility to fine-tune the thin film deposition [9]. In APP-based deposition, an organometallic precursor is transferred by a carrier gas and mixed in the feed gas. This mixture is then injected into the plasma (e.g. discharge region), where a reactive gas (in this case oxygen and ammonia) is added. Reactive species are formed from the feed gas, the reactive gas, and the precursor. The decomposed precursor is then deposited on the desired substrate [10]. Significant advances have been achieved in the last years towards the fabrication of TiO_2 thin films by APP techniques [9]. First, different Ti-based precursors solutions are commonly used including titanium chloride ($TiCl_4$) [11] and titanium tetraisopropoxide (TTIP, $Ti[OCH(CH_3)_2]_4$) [12]. However, the former produces toxic byproducts and chlorine contamination in the film making TTIP the most widely used compound since TTIP is much

* Corresponding author at: Chemistry of Surfaces, Interfaces and Nanomaterials, cp 255, Faculty of Sciences, Université libre de Bruxelles, 50 Avenue F.D. Roosevelt, 1050 Brussels, Belgium.
E-mail address: adrien.chauvin@umons.ac.be (A. Chauvin).

https://doi.org/10.1016/j.surfcoat.2023.129936
Received 16 June 2023; Received in revised form 18 August 2023; Accepted 20 August 2023
Available online 21 August 2023

more environmentally benign. Then, different plasma generation methods have been used for the synthesis of TiO_2 thin film by APP including dielectric barrier discharges (DBDs) [13], radiofrequency (RF) [14], and microwave (MW)-driven plasmas [15]. The integration of the plasma generation in deposition devices allows for the design of two main systems namely the classical parallel-plate DBD system or plasma jet (or plasma torch) system. In the first approach, (i.e. direct approach), the substrate is placed between the electrodes and is, therefore, directly exposed to the plasma [16] while, in the second approach (i.e. remote approach), the substrate is located downstream of the plasma generation region [17]. The main drawback in APP processes relies on the short mean free path of reactive species (a few micrometers) compared to those at low-pressure plasmas (several millimeters), which consequently results in the poorly controlled synthesis of the films [16]. Thus, to obtain thin films with the desired surface morphology and composition, systematic control of the operating conditions is essential. There are a large number of synthesis parameters affecting film synthesis, e.g., input power [13], frequency [18,19], gas composition [13,20], substrate surface characteristics [21], and substrate temperature [22]. Besides significant advances in the APP-DBD approach, some questions remain unsolved since no in-depth analysis of the effects of these various deposition parameters on the composition, morphology, and optical properties is reported. Moreover, most of the depositions have been carried out at ambient temperature. Thus, only amorphous TiO_2 was synthesized after deposition and thermal post-treatment was therefore mandatory to obtain crystalline TiO_2 thin films. In addition, the doping of TiO_x by nitrogen during the APP deposition has not been explored in detail so far.

In this study, we report the synthesis of TiO_x and TiO_x doped with nitrogen (TiO_x-N) by the AP-DBD approach. A rigorous analysis of the influence of the feed gas composition, the power, and the temperature of the substrate on the morphology, thin film composition, and optical properties of the film is reported.

2. Experimental

2.1. Synthesis of TiO_x and TiO_x-N thin film

The experimental setup is described in detail elsewhere [13,23]. Briefly, the plasma reactor is a homemade DBD reactor composed of a glass chamber with an inner diameter of 210 mm. The plasma is generated between two copper electrodes covered with a 3 mm thick alumina barrier. The gap between the electrodes was fixed to 3 mm. An AFS G10S-V AC power supply, operating at 2.7 kHz, is connected to the high-voltage electrode. A homemade induction system, described in detail elsewhere [24], allows the heating of the sample holder. The temperature of the sample holder was calibrated using an infrared camera. Silicon (001) and borosilicate glass has been chosen as substrate depending on the analysis conducted afterward. The substrate is first cleaned with isopropanol and methanol before each deposition. First, the chamber is pumped down to a pressure below 10 Torr and then backfilled with Ar at atmospheric pressure to avoid air contamination. TTIP (Titanium isopropoxide, 97 %, Sigma Aldrich) has been used as the precursor. TTIP is heated at 343 K and introduced in the chamber via a bubbler and a 1 slm Ar flux. The pipeline between the bubbler and the chamber is heated at 363 K (measured with a thermocouple during the synthesis). During the deposition, the total gas flow is fixed to 10 slm. The O_2 concentration in the injected gas is tuned between 5 and 20 vol% (i.e. 0.5 to 2 slm, respectively), and the NH_3 concentration between 0.9 and 9.4 vol% (i.e. 0.09 to 0.94 slm, respectively). The applied power is tuned between 15 and 75 W and the deposition time is fixed to 10 min. The values of power reported in the manuscript correspond to the one applied from the generator.

2.2. Characterization

Scanning electron microscopy (SEM) is performed in a HITACHI STEM-FEG with an acceleration voltage of 3 kV. The images were treated with ImageJ software to assess the thickness of the film. Each thickness has been measured 50 times in different SEM images taken in different positions over the sample. The XPS analysis is performed in a PHI 5000 VersaProbe with a monochromatic Al Kα (1486.7 eV) X-ray source. The survey and the high-resolution zone spectra have been recorded with a pass energy of 187.85 eV and 23.5 eV respectively. The spectra are calibrated with the C1s peak at 284.8 eV. Multipack software was used for the analysis composition while CasaXPS for the fitting of the peak. The UV–visible measurement is performed on a Cary 500 UV equipped with an integration sphere of 150 mm in diameter. The Raman analysis is performed in a Senterra Bruker micro-Raman system spectrometer with a laser wavelength of 532 nm, an objective x50, a power of 5 mW, and an integration time of 5 s with 5 repetitions. Near-edge X-ray absorption fine structure (NEXAFS) was recorded at the PEEM/XAS beamline (photon energy range of 200–2000 eV) of the SOLARIS Synchrotron (Krakow—Poland) [25]. NEXAFS measurements were carried out in partial fluorescence yield (PFY) at room temperature.

3. Results and discussion

3.1. Characterization of TiO_x thin films

3.1.1. Influence of the substrate temperature

First, we study the effect of substrate temperature on TiO_x thin film properties. In our previous study, the deposition of TiO_x by DBD at atmospheric pressure and ambient temperature results in a high-speed deposition of TiO_x film made of nanoparticles which can be crystalized by a post-annealing step into the anatase phase [26]. Then, when the deposition is carried out in the same condition, we showed that the morphology can be tuned with the energy density of the plasma from a granular to a dense film [13]. Besides a fine control of the morphology, no crystalline TiO_2 structure has been reported after deposition. Recently, the heating of the substrate during the deposition at 673 K has been used to allow a spontaneous crystallization of the TiO_x film [24]. However, no insight into the evolution of the composition of the film has been reported. Thus, the substrate temperature (T_{sub}) during the deposition was tuned from ambient temperature to 673 K, i.e. ambient, 373, 473, 573, and 673 K, and the chemistry of the film was evaluated by XPS. During the heating experiment, the power (P_{in}) was fixed to 45 W and the O_2 ratio (Φ_{O2}) to 10 vol%.

The evaluation of the film composition reveals a stable carbon content near 20 at.% for all T_{sub}. The O 1 s peak (Fig. 1a) shows two components situated at 531.8 and 530.1 eV corresponding to O—H and Ti—O bounding. Then the Ti $2p_{3/2}$ peak (Fig. 1b) is characterized by an intense component centered at 458.8 eV, attributed to $Ti^{4+,}$ and a low-intensity component at 457.0 eV attributed to Ti^{3+} (Inset Fig. 1b); this component contributes with <3 % to the total intensity of the Ti $2p_{1/2}$ peak). Finally, the C1s peak (Fig. 1c) reveals 3 components situated at 284.9, 286.5, and 289 eV corresponding to C—C, C—O, and C═O bounding [12,27,28]. When increasing T_{sub}, a decrease in the intensity of the O—H, C═O, and C—O components is observed. Compounds like hydroxyl groups are more likely to become incorporated at low T_{sub} as they are more volatile at higher T_{sub} [29]. According to the Wagner plot (Fig. 1d), one can see the increase of the Ti LMM Auger peak position towards higher kinetic energy when increasing T_{sub} leading to an increase of the Ti Auger parameter (α'). This can be associated with an increase in the crystallite size and percentage of crystalline phases [30]. Moreover, the FWHM of the Ti $2p_{3/2}$ peak decreases from 1.62 to 1.31 when increasing T_{sub} from ambient to 573 K and then becomes constant. This could be linked to the fingerprint of a higher degree of order [31]. Overall, it appears that the increase of T_{sub} likely allows for a better crystallization of the thin film. Thus, in the next section, T_{sub} is fixed to

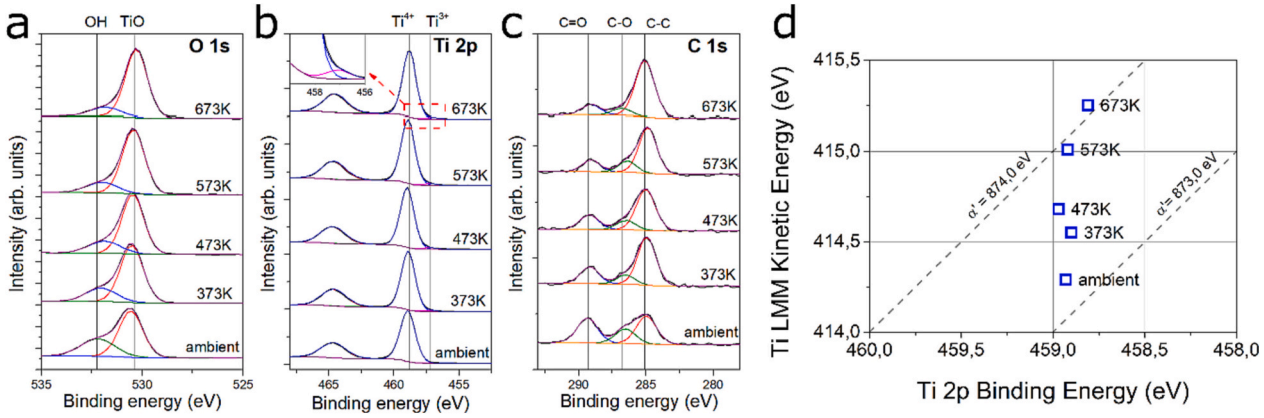

Fig. 1. XPS core level spectra and fitting of TiO_x sample deposited at P_{in} = 45 W, Φ_{O2} = 10 vol%, and for T_{sub} = ambient, 373, 473, 573, and 673 K including (a) O 1 s, (b) Ti 2p and (c) C 1 s. (d) Wagner plot of the TiO_x samples for different T_{sub}. The inset of b highlights the Ti^{3+} component in the Ti $2p_{3/2}$ peak.

673 K.

3.1.2. *Influence of the O_2 concentration*

To evaluate the influence of the different parameters on the morphology and the structure of the film, the composition of the gas was first studied. For this purpose, P_{in} was fixed to 45 W. The total flow was fixed to 10 slm and four O_2 flows were selected, i.e. 0.5, 1, 1.5, and 2 slm corresponding to Φ_{O2} = 5, 10, 15, and 20 vol%, respectively.

The SEM images (Fig. 2) show the evolution of the morphology of the film when increasing Φ_{O2}. First, one can see a cauliflower-like structure for all samples (Fig. 2a-d). This structure is characteristic of the deposition by APP PECVD [32,33] and is linked to a fast depletion of the precursor in the gas phase. This depletion induces the formation of nanoparticles in the gas phase, which will then agglomerate on the substrate [33]. For low Φ_{O2} (i.e. below 15 vol%) these agglomerates (Fig. 2a, b, and c) become thinner with increasing Φ_{O2}. Indeed, increasing Φ_{O2} leads to more effective carbon removal during the deposition and ultimately to thinner agglomerates [12,20]. This observation is correlated with the appearance of a porous morphology along the thickness of the sample (Fig. 2e, f, and g). Meanwhile, when the Φ_{O2} = 20 vol%, the agglomerates start vanishing (Fig. 2d), and the thin film becomes denser (Fig. 2h). By increasing the Φ_{O2}, a decrease in the thickness of the thin film from ~900 to 400 nm is observed. To support this observation, an XPS analysis was carried out.

The composition evaluated by XPS (Fig. SI1 and Fig. 3a), shows a decrease of the carbon amount on the sample surface from 19 at.% to 7 at.% when Φ_{O2} increases from 5 to 20 vol%. The carbon amount detected includes remaining from the deposition and storage. To limit the post-deposition contamination the plasma was running without injecting the precursor for 2 min after the deposition. The evolution of the carbon content when tuning Φ_{O2} has been discussed in the literature. First, Shelemin et al. reported that adding 20 vol% of Φ_{O2} in a TTIP/N_2 discharge leads to a decrease in the carbon content from 37 at.% to 23 at.% [12]. Moreover, Kang et al. showed by adding only 0.5 vol% of Φ_{O2} in a TTIP/He discharge that the amount of carbon decreases from 30 at.% to 7 at.% [28]. Thus, the addition of O_2 in the discharge promotes a decrease in the carbon content of the coating. Then, Aghaee et al. show that the increase from 15 to 30 vol% of Φ_{O2} to the TTIP/N_2 plasma leads to a gradual decrease in the carbon content from 10.1 at.% to <5 at.% [21]. However, Klenko et al. highlight no change in the carbon content of the TiO_2 when tuning the Φ_{O2} between 45 and 75 vol% in a TTIP/Ar discharge with around 35 at.% residue [20]. Thus, it seems that increasing Φ_{O2} leads to a decrease in the carbon content up to a certain limit. In our studies, with Φ_{O2} = 20 vol%, in the TTIP/Ar discharge, the carbon residue in our samples (around 7 at.%) is one of the lowest reported in the literature for AP-DBD. The ratio of O/Ti was 1.8 and did not vary when the Φ_{O2} was varied. From the detailed XPS analysis, one can highlight changes in the amount of oxygen vacancy (V_O); evaluated with the ratio between the area under the Ti^{3+} and Ti^{4+} components in the Ti $2p^{3/2}$ peak (Fig. SI1) assuming that an oxygen vacancy leads to two Ti^{3+} ions to maintain the electrostatic balance [34]; for increasing Φ_{O2}. The evolution of V_O for the different Φ_{O2} is plotted in Fig. 3a. The

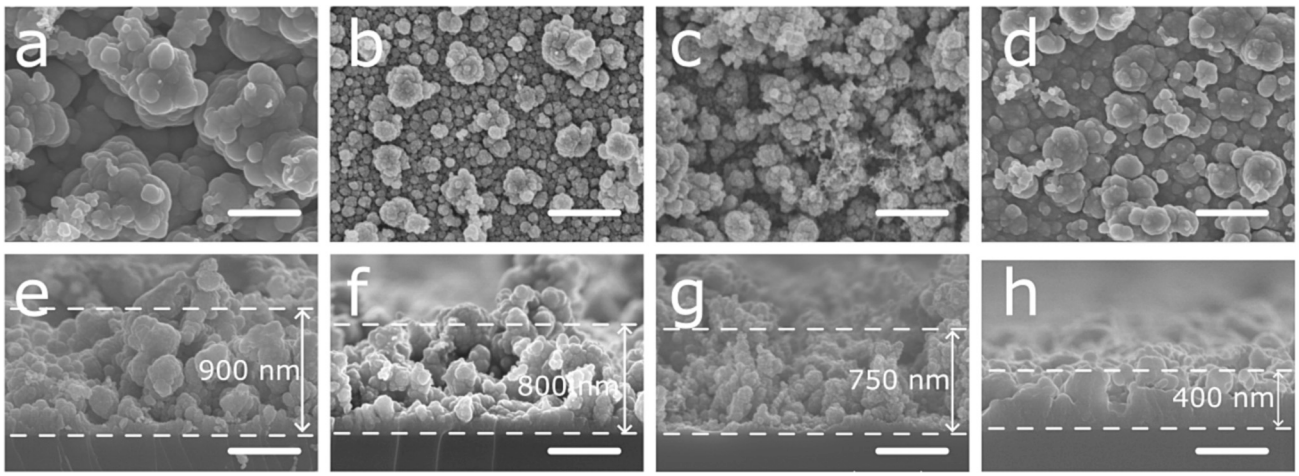

Fig. 2. (a-d) Plan view and (e-h) cross-section SEM of the morphology of the TiO_x thin films deposited with P_{in} = 45 W, a total flow of 10 slm, and with an Φ_{O2} = (a,e) 5 vol%, (b,f) 10 vol%, (c,g) 15 vol% and (d,h) 20 vol%. Scale bar: 500 nm.

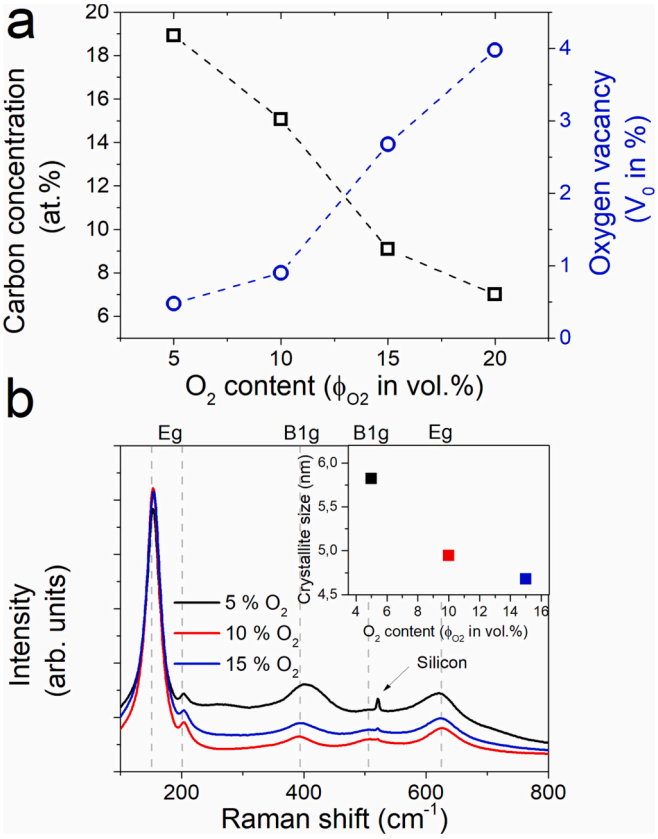

Fig. 3. (a) Composition of the TiO_x thin film deposited with a P_{in} = 45 W, a total flow of 10 slm, and with Φ_{O2} = 5, 10, 15, and 20 vol% evaluated by XPS. (b) Raman spectra and (Inset of (b)) crystallite size of thin film deposited with Φ_{O2} = 5, 10, and 15 vol%.

amount of V_O increases when increasing Φ_{O2} this could be correlated to the crystalline quality of the material since the formation of V_O is common in amorphous TiO_2 since it is energetically more favorable than in crystalline TiO_2 [35]. To evaluate the crystallinity of the films, Raman spectra have been recorded on the films synthesized for each Φ_{O2} (Fig. 3b). It is important to stress here that no X-ray diffraction (XRD) signal has been detected when analyzing these samples. The presence of anatase crystallite in the film deposited with low Φ_{O2} is revealed since the bands at 143 cm^{-1}, 197 cm^{-1}, 397 cm^{-1}, 516 cm^{-1}, and 638 cm^{-1} are the fingerprint of TiO_2 anatase [36]. The presence of the anatase crystallite on the Raman pattern and not on the XRD one is due to the non-homogeneous structure of the sample. Indeed, the Raman patterns are recorded on the cauliflowers-like agglomerates that are constituted of crystalline structures [33]. For samples deposited with higher Φ_{O2}, no Raman signal has been detected. The crystallite size, L, can be evaluated by the variation of the position, Δω, and the line width at half maximum, Γ, of the main Raman band with the relations:

$$\Delta\omega = k_1\left(\frac{1}{L^\alpha}\right) \quad (1)$$

$$\Gamma = k_2\left(\frac{1}{L^\alpha}\right) + \Gamma_0 \quad (2)$$

with $k_1 = 142.5$, $k_2 = 180$, and $\Gamma_0 = 9.94$. α is a scaling parameter of 1.5 [37,38]. This approximation is well adapted for crystallite size below 10 nm [39,40]. The values of Γ and Δω are evaluated by Gaussian fit of the peak at 144 cm^{-1}. The inset of Fig. 3b displays the crystallite size of the TiO_2 anatase obtained by Raman. When increasing Φ_{O2} from 5 to 15 vol %, a slight decrease in the crystallite size is observed from 5.8 to 4.7 nm, respectively. Besides decreasing the crystallite size of the thin film, increasing Φ_{O2} leads to a decrease in the amount of residual carbon and an increase in V_O.

3.1.3. *Influence of the power*

P_{in} is also an important parameter allowing for tuning the morphology [13,26]. In this study, T_{sub} and Φ_{O2} have been fixed to 673 K and 10 vol%, respectively, whereas P_{in} has been tuned between 15 and 60 W. Indeed when P_{in} > 60 W, arcs have been observed.

The SEM images of the thin film deposited for the different P_{in} are displayed in Fig. 4. For a sample made with P_{in} = 15 W (Fig. 4a and e), the film is very thin (<150 nm). In this case, due to the low P_{in}, a lower amount of electrons are available to dissociate the precursor, thus the deposition speed is slower. When P_{in} = 30 W, the film presents a dense morphology (Fig. 4b, f). When P_{in} = 45 W, the film becomes porous with a more visible cauliflowers-like structure (Fig. 4c and g). Finally, for P_{in} = 60 W, the porous morphology is even more obvious, and the film consists of aggregations of nanoparticles (Fig. 4d and h) as mentioned previously. When comparing the morphology of these films, deposited at 673 K, with the one reported in the literature for a deposition at ambient temperature, no notable difference can be reported [13]. The film deposited at low power is dense while the one deposited at high power is porous. Indeed, for low-power regimes, the film appears more compact since it is likely constituted aggregate of nanoparticles with a core–shell structure where a plasma polymer phase grows around a TiO_2 cluster [12].

The chemical composition and the structure of the film surface were analyzed by XPS (Fig. 5a) and Raman (Fig. 5b), respectively. The concentration of carbon on the surface of the thin film deposited at 15 W is 23 at.% indicating a high content of residue from the precursor. Then, the concentration of carbon contamination decreases to 15 at.% for P_{in} = 30 W along with the appearance of a weak Raman signal corresponding to TiO_2 anatase. The concentration of residual carbon remains constant for P_{in} = 45 W, while the Raman signal of the anatase phase is observed. Finally, for P_{in} = 60 W, the concentration of carbon slightly decreased to reach 12 at.% and the Raman signal of anatase is visible. The decrease in the carbon residue of the film is coherent with the literature since the energy density per molecule increases when increasing the power [12]. In the low-pressure plasma polymerization process, this can be evaluated by the Yasuda factor [41]. The Yasuda parameter shows a correlation between the discharge power (P) and the flow rate (F). At high P/F, the film is more inorganic, whereas, when the ratio P/F is low, the film turns out to be more organic [12]. This behavior agrees with our observations since the precursor flow rate is similar for all samples and only the power is tuned. The XPS analysis reveals a decrease of the O/Ti ratio when increasing the power going from an over-stochiometric film at P_{in} = 30 W to a sub-stoichiometric film for P_{in} above 45 W. This observation could be explained by the stronger dissociation of oxygen when increasing P_{in}. The amount of V_O in the thin film is constant for the different P_{in} at around 1 %. The Raman analysis of the sample deposited at the different P_{in} highlights the slight increase of the crystallite size from 4.7 to 5.2 nm when increasing P_{in} from 30 to 60 W, respectively. Therefore, we conclude that increasing P_{in} leads to a strong modification of the morphology from a dense to a porous film. Moreover, it also allows the growth of bigger crystallites together with a slight decrease in the carbon residue.

3.2. *Doping of the TiO_x thin film*

The deposition of TiO_x thin film has been carried out by adding NH_3 in the injected gas aiming to dope the TiO_x to reduce its bandgap. This would allow the utilization of a wider range of the solar spectrum to activate the photocatalytic activity of the material. Indeed, TiO_2 has an intrinsic wide bandgap that limits the excitation to the UV range, corresponding to around 5 % of the solar spectrum.

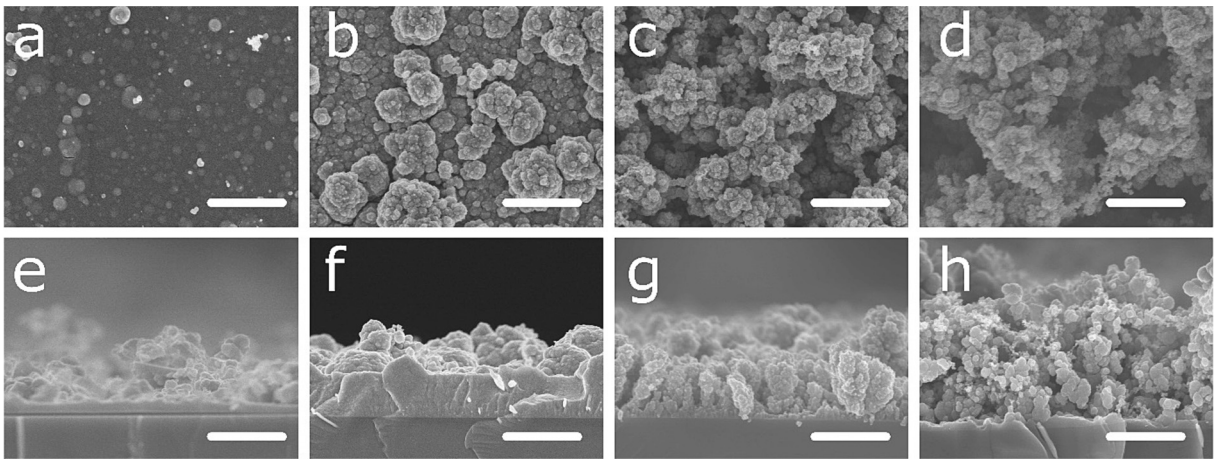

Fig. 4. (a-d) Plan view and (e-h) cross-section SEM of the morphology of the TiO_x thin films deposited with $\Phi_{O2} = 10$ vol% and P_{in} of (a, e) 15 W, (b, f) 30 W, (c, g) 45 W, and (d, h) 60 W and $T_{sub} = 673$ K. Scale bar: 1 μm.

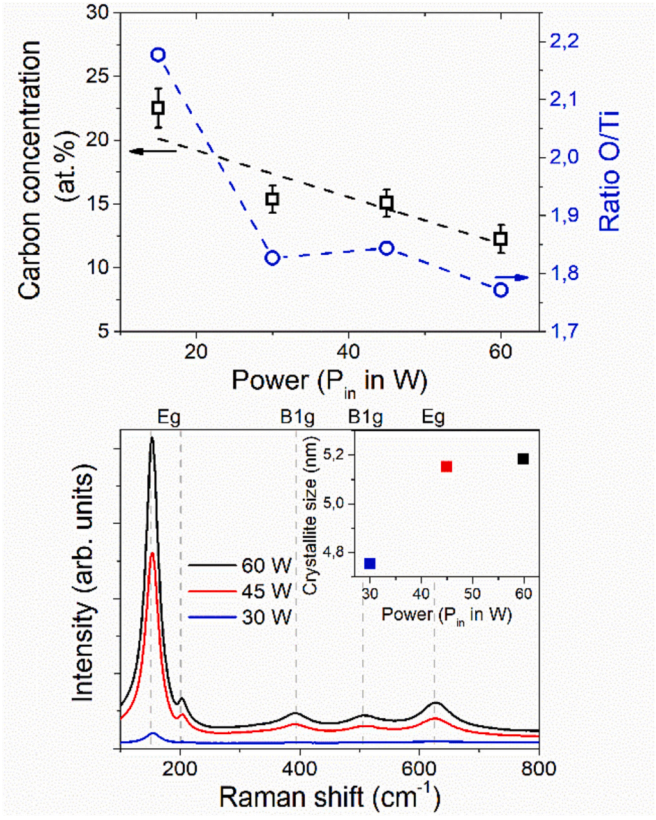

Fig. 5. (a) Evolution of carbon concentration and the ratio O/Ti, evaluated by XPS, of the TiO_x thin film deposited with an $\Phi_{O2} = 10$ vol%, a total flow of 10 slm, and $P_{in} = 15$ W, 30 W, 45 W, and 60 W. (b) Raman spectra and (Inset of (b)) crystallite size of thin film deposited with $P_{in} = 30$ W, 45 W, and 60 W.

3.2.1. *Influence of the substrate temperature*

Compared to previous studies reporting the synthesis of N-doped TiO_2 [12,23], our films have been heated at different temperatures (373 K to 673 K) during their growth. The influence of T_{sub} on the composition has been studied keeping the other parameters constant (i.e. $\Phi_{O2} = 5$ vol%, $\Phi_{NH3} = 1.8$ vol%, a total flow of 10 slm, and $P_{in} = 45$ W).

Fig. 6 shows the evolution of the O 1 s, Ti 2p, and N 1 s XPS peaks for different T_{sub}. Without heating, the O 1 s peak has to be fitted with one more component than in the XPS spectrum shown in Fig. 1a. This peak, located at 533.5 eV, corresponds to O—C groups. When T_{sub} increases, this peak disappears and, as observed for the TiO_x samples (Fig. 1a), a decrease in the intensity of the OH component can be observed and explained by the promotion of the desorption of hydroxyl groups when increasing T_{sub}. The Ti $2p_{3/2}$ peak can be fitted using two components including Ti^{4+} at 458.8 eV and Ti^{3+} located at a lower binding energy, i.e. 457 eV. When increasing T_{sub}, the amount of V_O increases as discussed before. Then, the FWHM of the Ti $2p_{3/2}$ peak follows a behavior similar to the one reported for the TiO_x, i.e. going from 1.75 to 1.31 for T_{sub} from ambient to 673 K, respectively. Therefore, a higher order is expected in the film deposited at higher T_{sub}. The N 1s peak of the sample prepared without heating contains three contributions The component located at 400 eV which can be assigned to interstitial nitrogen in the TiO_x structure is observed for all samples [42]. Then, a component at high binding energy (i.e. 407.1 eV) that could be assigned to nitrate compounds [21] tends to vanish when increasing T_{sub}. This can be understood as follows: nitrate compounds can be created by the degradation of NO gas considering the photocatalysis process on TiO_2 [43] which would be activated by the light emitted from the plasma. Nevertheless, when increasing T_{sub}, the nitrate compound disappears since they are unstable under heating and tends to decompose in NO. Then a second component at 401.7 eV could be assigned to N_2 [42,44]. This component is present for all deposition conditions and decreases when increasing T_{sub}. To support this hypothesis NEXAFS analysis was performed on the samples (Fig. 7).

As NEXAFS spectroscopy probes the electronic structure of the material, we evaluate the presence of different N-bonding environments to verify the XPS analysis. Spectral features are given based on their similarities to the NEXAFS spectra reported for molecular nitrogen and inorganic nitrate salts [45–49]. The N K-edge spectrum (Fig. 7) shows a broad low-intensity band centered at 401 eV. To examine in detail this region of the spectrum, we recorded a spectrum in the 400–402.5 eV photon energy range with 0.1 eV of step energy (inset of Fig. 7), and the observed peaks are characteristic of N_2 molecules [45,50,51]. The set of peaks observed in this energy range is a fingerprint of the N_2 molecule due to its vibrational structure [51]. The peak centered at 400.8 eV is assigned to the transition from the N 1 s electronic state to π^* orbital [51]. The observed fine structure in the N K-edge undoubtedly proves the presence of N_2 molecules in the N-doped TiO_2 sample. This behavior agrees with reported DFT calculations showing that nitrogen atoms in TiO_2 are energetically unstable and spontaneously form trapped or gaseous N_2 [52]. The narrow band centered at 404.8 eV was reported to arise from transitions of the N 1s level to the $2a2''$ (π^*) LUMO orbital of NO^{3-} anion [47]. At higher photon energy, a broad featureless band from 410 to 420 eV was reported to be generated from N 1 s transitions to the $5a1'$ ($\sigma^*N - O$) and doubly degenerated 5e' ($\sigma^*N - O$) orbitals of

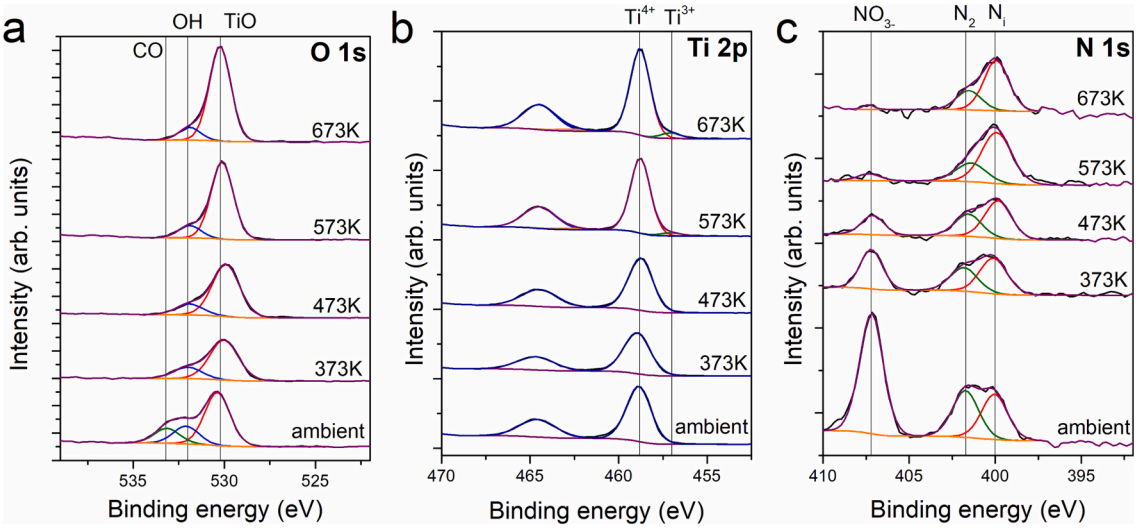

Fig. 6. XPS core level spectra and fitting of N-TiO_x sample deposited at P_{in} = 45 W, Φ_{O2} = 5 vol%, Φ_{NH3} = 1.8 vol%, and T_{sub} = ambient, 373, 473, 573, and 673 K including (a) O 1 s, (b) Ti 2p and (c) N 1 s.

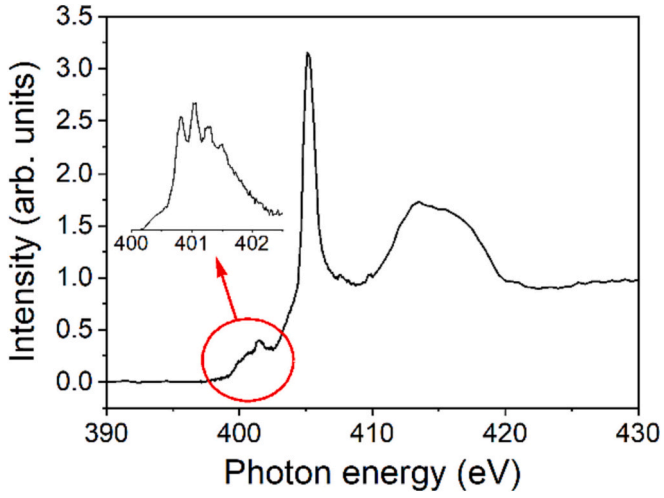

Fig. 7. NEXAFS of the N K-edge of N-TiO_x sample deposited with P_{in} = 45 W, Φ_{O2} = 5 vol%, Φ_{NH3} = 1.8 vol%, and T_{sub} = 373 K.

NO^{3-} [50]. The presence of nitrogen in different chemical environments was confirmed by XPS measurements (Fig. 6c), which agree with previous XPS studies of nitrogen-doped TiO_2 [42]. Overall, the increase in T_{sub} when adding NH_3 in the working gas leads to N-TiO_x thin films with a higher amount of V_O compared to the samples deposited without NH_3. The interstitial nitrogen (N_i) in the structure represents 1.8 at.% for all T_{sub}. In line with the results mentioned earlier for thin films without NH_3, the Wagner plot reveals an increase of α' when increasing T_{sub} (Fig. SI2), thus an increase in the crystallite size can be expected. Moreover, less carbon residue is observed for T_{sub} = 673 K.

3.2.2. *Influence of the NH_3 flow*

The influence of Φ_{NH3} has been evaluated by keeping Φ_{O2} = 5 vol% and P_{in} = 45 W. Four NH_3 flows have been selected to reach Φ_{NH3} = 0.9, 1.8, 5.8, and 9.6 vol%.

The SEM images of the film deposited by tunning Φ_{NH3} are shown in Fig. 8. When Φ_{NH3} = 0.9 vol%, a structure composed of large aggregates generating porosity is observed (Fig. 8a and e). The morphology is similar to the one obtained without NH_3 (Fig. 4c, g). For Φ_{NH3} = 1.8 vol %, the size of the agglomerates reduces while keeping the porosity (Fig. 8b, f). When further increasing Φ_{NH3}, the film becomes dense (Fig. 8g and h) and an increase in the size of the agglomerates can be

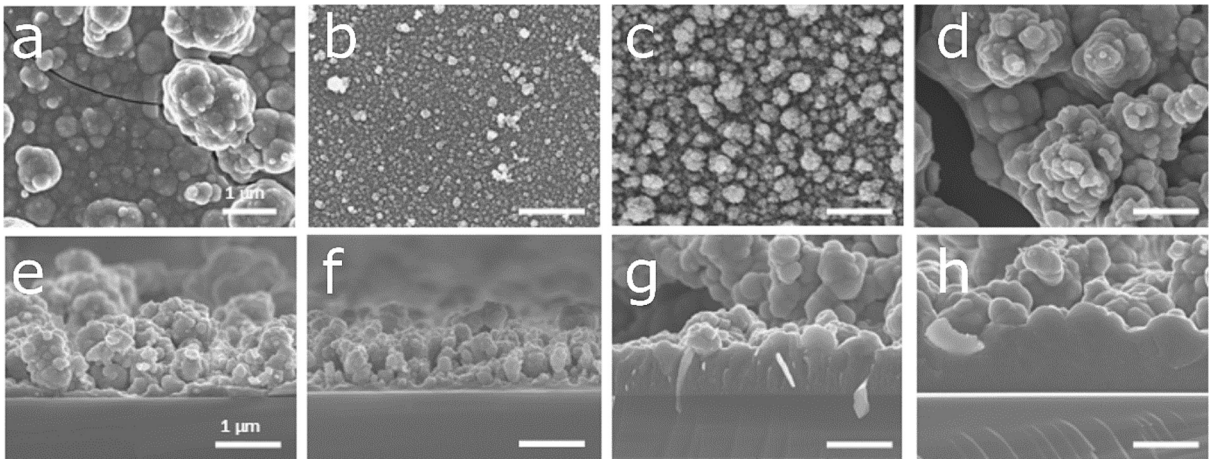

Fig. 8. (a-d) Plan view and (e-h) cross-section SEM of the morphology of the N-TiO_x thin film deposited with an Φ_{O2} = 5 vol%, P_{in} = 45 W, and Φ_{NH3} = (a, e) 0.9, (b, f) 1.8, (c, g) 5.8, (d, h) 9.6 vol%. Scale bar: 1 µm.

seen between 1.8 and 9.6 vol% (Fig. 8b, c, and d). It is interesting to point out that when increasing the amount of reactive gas (either O_2 or NH_3) and keeping the other parameters constant, the same morphological evolution is observed going from a porous to a more compact coating (Figs. 2 and 8). The composition of the thin film obtained by XPS (Fig. SI3) shows a similar amount of nitrogen in the thin film for all the conditions, i.e. 2 at.%, with no change in the peak shape. Moreover, the N_i and the V_O density are constant at ~0.7 and ~0.6 % respectively. Therefore, we can conclude that besides, affecting the morphology, the increase of the NH_3 content in the working gas does not change the composition of the thin film.

When tuning the other parameters such as Φ_{O2} or P_{in} in the presence of NH_3 in the working gas, a similar evolution of the morphology to the one observed for TiO_x films is observed. The thin film prepared at low P_{in} exhibit a denser structure than the one made at high P_{in} (Fig. SI4). No changes in morphology were observed for the thin film deposited with a different Φ_{O2}. The variation in the film composition follows the same trend as the one observed for the undoped thin films when Φ_{O2} was varied: the increase of Φ_{O2} increases the amount of V_O in the thin film until reaching 4.2 % for $\Phi_{O2} = 20$ vol% (Fig. 9) similarly to the undoped case (Fig. 3a). The amount of N_i in the thin film increases up to 1.15 % for $\Phi_{O2} = 15$ vol% and then drops when reaching a higher Φ_{O2}. Overall the AP-DBD approach using NH_3 in the working gas allows the creation of N_i in the structure without modification of the morphology or composition. To tune the amount of N_i in the structure, one should vary with Φ_{O2}.

3.2.3. Bandgap analysis

The effect of nitrogen doping on the bandgap values of the TiO_x thin films is evaluated.

When the power reaches 75 W with $\Phi_{O2} = 5$ vol% and $\Phi_{NH3} = 1.8$ vol %, arcs avoid the preparation of samples similarly to Section 3.1.3. The arcing phenomenon is due to the high density of electrons in the discharge and it is linked to Paschen's law [53,54]. For a discharge in pure Ar, arcing is observed for low P_{in} (<45 W). When adding O_2 and/or NH_3 to the gas mixture, the electron density decreases and the limit for arcing is increasing. Thus, the arcing is only observed for low amounts of O_2 and/or NH_3 and high P_{in}.

The bandgap (Eg) has been evaluated by using the Tauc plot method [55,56]. It is important to note here that our samples have a significant absorption of sub-bandgap energy photons (Fig. SI5a). This can be due to defects, doping, bulk, or surface modification which can introduce intraband gap states that reflect light in the absorption spectrum [55]. It is, thus, important to take this parameter into account for the determination of Eg by the Tauc plot method since a direct application of the Tauc method would result in an inaccurate estimation of Eg as already seen in several publications. In our case, the 'baseline method' has been used. Briefly, by modeling and extrapolating a baseline signal tangent from the absorption value below the bandgap, one can estimate Eg with the intersection with the Tauc slope (Fig. SI5b) [55,56].

Besides a decrease of Eg when adding NH_3 in the gas mixture, even for a low amount (i.e. 0.9 vol%) going from 3.3 eV to 3.23 eV with $\Phi_{O2} = 10$ vol% and $P_{in} = 45$ W, no change can be seen when further increases Φ_{NH3} (Fig. SI6). This behavior can be related to the fact that increasing Φ_{NH3} during the deposition did not affect the composition. The decrease of Eg when adding NH_3 to the gas is likely linked to the addition of nitrogen in the TiO_x structure (Fig. SI3). The p orbitals of nitrogen contribute to the electronic bandgap narrowing by mixing with O2p orbitals. This leads to a shift of the absorption edge towards the visible range [57].

Following our observations, Φ_{O2} and P_{in} seem to have a significant impact on Eg. Fig. 10a shows the evolution of Eg as a function of the Φ_{O2} and P_{in} for samples prepared with $\Phi_{NH3} = 1.8$ vol%. First, no specific trend can be observed besides a decrease of Eg for P_{in} higher than 30 W. For $\Phi_{O2} = 5$ and 10 vol%, the lowest Eg is reported for $P_{in} = 45$ and 75 W while for $\Phi_{O2} = 15$ and 20 vol%, it is for 60 and 45 W. Then, turning Φ_{O2} leads to a stronger modification of the bandgap with a minimum of Eg for $\Phi_{O2} = 5$ and 10 vol%. To look into some possible explanations for the narrowing of Eg, an insight into the composition of the films has been carried out by XPS (Fig. S7, Fig. 10b, and c). First, the importance of adding O_2 to the gas is highlighted by the drop in the O/Ti ratio with only $\Phi_{O2} = 5$ vol% (Fig. SI7). The high value of the O/Ti ratio for the coating made without oxygen in the gas mixture highlights the low dissociation rate of the precursor. Oxygen species are highly reactive and will create volatile compounds which will allow the removal of the remaining carbon from the precursor [12]. An explanation arises from the different amounts of dopant in the coating together with the different amounts of V_O. N doping of TiO_2 is always accompanied by oxygen vacancies (V_O). The charge imbalance between N^{3-} and O^{2-} can be compensated by the Ti^{3+} ions of V_O. In this case, the N dopant can gain electrons via charge transfer from Ti^{3+} ions increasing the occupation number of electrons in the N2p states. Thus, different N/V_O dopants lead to different electronic properties [58–61]. To follow the influence of the N doping, N_i content has been reported for the different conditions (Fig. 10b). N_i increases when increasing P_{in} and Φ_{O2} in the gas mixture (except for $P_{in} = 30$ W). Then, the amount of V_O was followed for the different P_{in} and Φ_{O2} (Fig. 10c). One can see a different behavior for V_O compared to the case of undoped TiO_x (Fig. 3a). In the case of N-TiO_x, for all P_{in}, the amount of V_O is constant when tuning the Φ_{O2} until 10 vol% followed by a decrease for higher Φ_{O2}. The amount of V_O can be correlated to the Eg since the minimum bandgap is also reported for $\Phi_{O2} = 5$ and 10 vol% (Fig. 10a). However, the amount of V_O only cannot fully explain the evolution of Eg, thus a balance between a high amount of N_i together with a high amount of V_O has to be reached to get a low Eg. Further work will focus on the determination of the valence band position to propose a band structure of the TiO_x coating and highlight the impact of the N-doping [62].

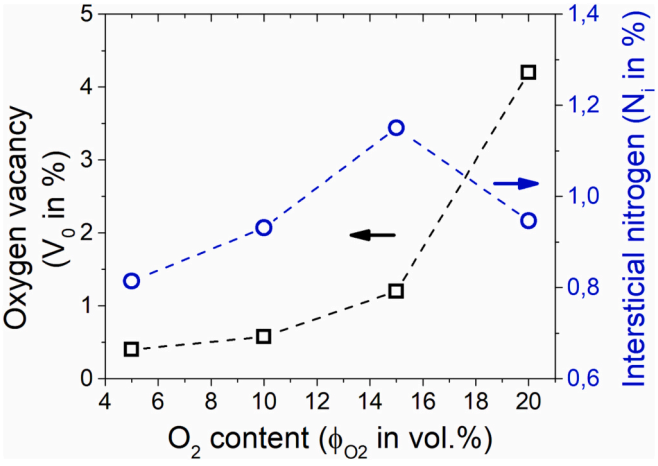

Fig. 9. Amount of V_O and N_i evaluated by XPS of the N-TiO_x thin film deposited with $P_{in} = 45$ W, a total flow of 10 slm, $\Phi_{NH3} = 1.8$ vol%, and $\Phi_{O2} = 5$ vol%, 10 vol%, 15 vol%, and 20 vol%.

4. Conclusion

The deposition of TiO_x and N-TiO_x by AP-DBD has been reported to be an efficient way to tune the morphology and structure of the thin film. The deposition by AP-DBD with heating the substrate at 673 K has proven its ability to reduce carbon contamination in the thin film and to promote larger anatase crystallites within the film compared to the one deposited at ambient temperature. The increase of the Φ_{O2} allows for a denser film, and a lower amount of carbon residue together with an increase of V_O, however, it also decreases the crystallite size. The increase of P_{in} (in the range of 30 W to 75 W) leads to a switch from a dense to a porous film. It also increases the crystallite size and slightly

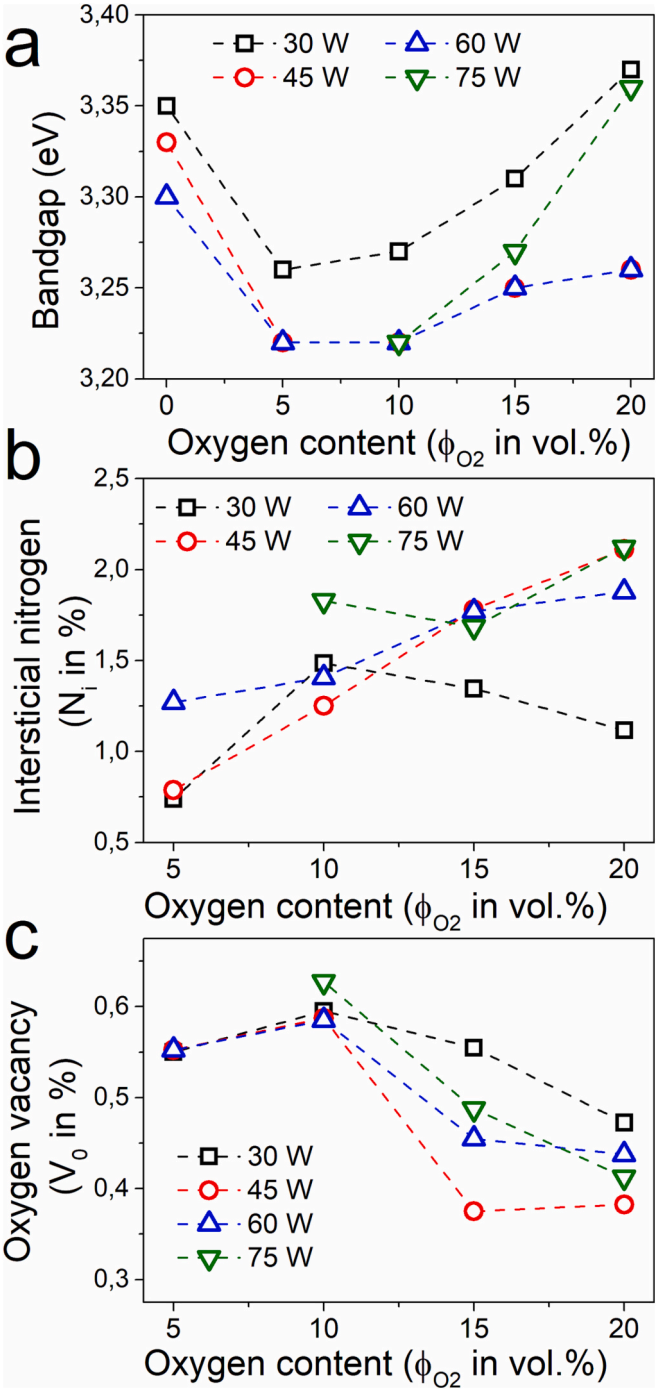

Fig. 10. (a) Bandgap of the N-TiO_x thin film deposited with Φ_{NH3} = 1.8 vol% and for different Φ_{O2} and P_{in}. For better visibility, the standard deviation has been removed and corresponds to 0.02 eV. Evaluation of the (b) N_i ratio, (c) V_O for the samples deposited with Φ_{NH3} = 1.8 vol% for different Φ_{O2} and for P_{in} = (black square) 30 W, (red circle) 45 W, (blue triangle), 60 W and (green diamond) 75 W.

decreases the carbon residue. Adding NH_3 to the working gas allows the effective doping of the structure by interstitial nitrogen. When increasing Φ_{NH3}, the film becomes denser without modifying the composition. To increase the N_i in the film, one needs to increase Φ_{O2} and P_{in}. The optical evaluation of the energy bandgap reveals that the Φ_{O2} and P_{in} have affected the value of the bandgap. The lowest value of Eg, i.e. 3.22 eV, was observed for the Φ_{O2} of 5–10 vol% when 1.8 vol% of ammonia was introduced into the gas mixture.

CRediT authorship contribution statement

Adrien Chauvin: Conceptualization, Methodology, Investigation, Formal analysis, Resources, Visualization, Writing – original draft, Writing – review & editing. **Carla Bittencourt:** Investigation, Data curation, Validation, Writing – original draft. **Mathilde Galais:** Investigation, Validation. **Lionel Sauvage:** Investigation, Validation. **Maxime Bellefroid:** Investigation, Validation. **Carine Van Lint:** Conceptualization, Resources, Validation, Supervision, Funding acquisition, Project administration, Writing – original draft. **Anne Op de Beeck:** Conceptualization, Resources, Validation, Supervision, Funding acquisition, Project administration, Writing – original draft. **Rony Snyders:** Conceptualization, Resources, Validation, Supervision, Funding acquisition, Project administration, Writing – original draft. **François Reniers:** Conceptualization, Resources, Validation, Supervision, Funding acquisition, Project administration, Writing – original draft, Writing – review & editing.

Declaration of competing interest

The authors declare that they have no known competing financial interests or personal relationships that could have appeared to influence the work reported in this paper.

Data availability

Data will be made available on request.

Acknowledgments

The authors gratefully acknowledge Y. Paint (Materia Nova, Mons), D. Cossement (Materia Nova, Mons), and X. Noirfalise (Materia Nova, Mons) for their technical assistance on the SEM, Raman, and the XPS, respectively. We would like to thank Dr. Marcin Zając (National Synchrotron Radiation Centre Solaris, Kraków, Poland) for assistance during the NEXAFS experiment. The laboratory of C.V.L. is part of the ULB-Cancer Research Centre (U-CRC). M.G. is a fellow of the EU Marie Skłodowska-Curie COFUND action (No 801505). M.B. is a doctoral fellow from the Belgian « Fonds pour la formation à la Recherche dans l'Industrie et dans l'Agriculture (FRIA-FNRS) ». CVL is « Directeur de Recherches » of the F.R.S-FNRS.

The authors thank the FNRS for the financial support through the "VirusSurf" project No H.P064.20. F.R., C.V.L., and A.O.D.B. thank the ULB-COVID-Fund. F.R. thanks the Jaumotte-Demoulin Foundation (ULB) for funding. C.B. is a Research Associate of the FRS-FNRS, Belgium. C.B. thank the Belgian Fund for Scientific Research under the FRFC contract EQP 40002995 (PHOTOFUN).

Appendix A. Supplementary data

Supplementary data to this article can be found online at https://doi.org/10.1016/j.surfcoat.2023.129936.

References

[1] X. Kang, S. Liu, Z. Dai, Y. He, X. Song, Z. Tan, Titanium dioxide: from engineering to applications, Catalysts 191 (2019) 32, https://doi.org/10.3390/catal9020191.
[2] A. Fujishima, T.N. Rao, D.A. Tryk, Titanium Dioxide Photocatalysis, 2000, p. 21.
[3] N. Rausch, E.P. Burte, Thin TiO2 films prepared by low pressure chemical vapor deposition, J. Electrochem. Soc. 140 (1993) 145–149, https://doi.org/10.1149/1.2056076.
[4] C. Su, B.-Y. Hong, C.-M. Tseng, Sol–gel preparation and photocatalysis of titanium dioxide, Catal. Today 96 (2004) 119–126, https://doi.org/10.1016/j.cattod.2004.06.132.
[5] W. Ravisy, M. Richard-Plouet, B. Dey, S. Bulou, P. Choquet, A. Granier, A. Goullet, Unveiling a critical thickness in photocatalytic TiO_2 thin films grown by plasma-enhanced chemical vapor deposition using real time in situ spectroscopic ellipsometry, J. Phys. D. Appl. Phys. 54 (2021), 445303, https://doi.org/10.1088/1361-6463/ac1ec1.

[6] D. Li, N. Gautier, B. Dey, S. Bulou, M. Richard-Plouet, W. Ravisy, A. Goullet, P. Choquet, A. Granier, TEM analysis of photocatalytic TiO2 thin films deposited on polymer substrates by low-temperature ICP-PECVD, Appl. Surf. Sci. 491 (2019) 116–122, https://doi.org/10.1016/j.apsusc.2019.06.045.

[7] A. Borrás, J. Cotrino, A.R. González-Elipe, Type of plasmas and microstructures of TiO2 thin films prepared by plasma enhanced chemical vapor deposition, J. Electrochem. Soc. 154 (2007) 6.

[8] A. Panepinto, Switching the electrical characteristics of TiO2 from n-type to p-type by ion implantation, Appl. Surf. Sci. 9 (2021).

[9] S. Banerjee, E. Adhikari, P. Sapkota, A. Sebastian, S. Ptasinska, Atmospheric Pressure Plasma Deposition of TiO2: A Review, 2020, p. 36.

[10] A. Sonnenfeld, T.M. Tun, L. Zajıc, Deposition process based on organosilicon precursors in dielectric barrier discharges at atmospheric pressure—a comparison, Plasmas Polym. 30 (2002).

[11] L.-B. Di, X.-S. Li, C. Shi, Y. Xu, D.-Z. Zhao, A.-M. Zhu, Atmospheric-pressure plasma CVD of TiO $_2$ photocatalytic films using surface dielectric barrier discharge, J. Phys. D. Appl. Phys. 42 (2009), 032001, https://doi.org/10.1088/0022-3727/42/3/032001.

[12] A. Shelemin, A. Choukourov, J. Kousal, D. Slavínská, H. Biederman, Nitrogen-doped TiO $_2$ nanoparticles and their composites with plasma polymer as deposited by atmospheric pressure DBD: nitrogen-doped TiO $_2$ nanoparticles and their composites …, Plasma Process. Polym. 11 (2014) 864–877, https://doi.org/10.1002/ppap.201300207.

[13] Q. Chen, Q. Liu, A. Ozkan, B. Chattopadhyay, G. Wallaert, K. Baert, H. Terryn, M.-P. Delplancke- Ogletree, Y. Geerts, F. Reniers, Atmospheric pressure dielectric barrier discharge synthesis of morphology-controllable TiO2 films with enhanced photocatalytic activity, Thin Solid Films 664 (2018) 90–99, https://doi.org/10.1016/j.tsf.2018.08.025.

[14] S. Collette, J. Hubert, A. Batan, K. Baert, M. Raes, I. Vandendael, A. Daniel, C. Archambeau, H. Terryn, F. Reniers, Photocatalytic TiO2 thin films synthesized by the post-discharge of an RF atmospheric plasma torch, Surf. Coat. Technol. 289 (2016) 172–178, https://doi.org/10.1016/j.surfcoat.2016.01.049.

[15] K. Baba, S. Bulou, P. Choquet, N.D. Boscher, Photocatalytic anatase TiO2 thin films on polymer optical fiber using atmospheric-pressure plasma, ACS Appl. Mater. Interfaces 9 (2017).

[16] F. Massines, C. Sarra-Bournet, F. Fanelli, N. Naudé, N. Gherardi, Atmospheric pressure low temperature direct plasma technology: status and challenges for thin film deposition, Plasma Process. Polym. 9 (2012) 1041–1073, https://doi.org/10.1002/ppap.201200029.

[17] A. Uricchio, F. Fanelli, Low-temperature atmospheric pressure plasma processes for the deposition of nanocomposite coatings, Processes. 9 (2021) 2069, https://doi.org/10.3390/pr9112069.

[18] J. Profili, S. Dap, O. Levasseur, N. Naude, A. Belinger, L. Stafford, N. Gherardi, Interaction of atomized colloid with an ac electric field in a dielectric barrier discharge reactor used for deposition of nanocomposite coatings, J. Phys. D. Appl. Phys. 50 (2017), 075201, https://doi.org/10.1088/1361-6463/aa515f.

[19] P. Brunet, R. Rincón, Z. Matouk, M. Chaker, F. Massines, Tailored waveform of dielectric barrier discharge to control composite thin film morphology, Langmuir 34 (2018) 1865–1872, https://doi.org/10.1021/acs.langmuir.7b03563.

[20] Y. Klenko, J. Pichal, TiOx films deposited by plasma enhanced chemical vapour deposition method in atmospheric dielectric barrier discharge plasma, Plasma Chem. Plasma Process. 32 (2012) 1215–1225, https://doi.org/10.1007/s11090-012-9401-0.

[21] M. Aghaee, J. Verheyen, A.A.E. Stevens, W.M.M. Kessels, M. Creatore, TiO2 Thin Film Patterns Prepared by Chemical Vapor Deposition and Atomic Layer Deposition Using an Atmospheric Pressure Microplasma Printer, (n.d.) 14.

[22] G.A. Battiston, R. Gerbasi, A. Gregori, M. Porchia, S. Cattarin, G.A. Rizzi, PECVD of amorphous TiO2 thin films: effect of growth temperature and plasma gas composition, Thin Solid Films 371 (2000) 126–131, https://doi.org/10.1016/S0040-6090(00)00998-6.

[23] Q. Chen, A. Ozkan, B. Chattopadhyay, K. Baert, C. Poleunis, A. Tromont, R. Snyders, A. Delcorte, H. Terryn, M.-P. Delplancke-Ogletree, Y.H. Geerts, F. Reniers, N-doped TiO $_2$ photocatalyst coatings synthesized by a cold atmospheric plasma, Langmuir. 35 (2019) 7161–7168, https://doi.org/10.1021/acs.langmuir.9b00784.

[24] A. Remy, M.S. Fall, T. Segato, S. Godet, M.P. Delplancke-Ogletree, P. Panini, Y. Geerts, F. Reniers, Improving the atmospheric plasma deposition of crystalline inorganic coatings, Thin Solid Films 688 (2019), 137437, https://doi.org/10.1016/j.tsf.2019.137437.

[25] M. Zając, T. Giela, K. Freindl, K. Kollbek, J. Korecki, E. Madej, K. Pitala, A. Kozioł-Rachwał, M. Sikora, N. Spiridis, J. Stępień, A. Szkudlarek, M. Ślęzak, T. Ślęzak, D. Wilgocka-Ślęzak, The first experimental results from the 04BM (PEEM/XAS) beamline at Solaris, Nucl. Instrum. Methods Phys. Res. Sect. B Beam Interact. Mater. At. 492 (2021) 43–48, https://doi.org/10.1016/j.nimb.2020.12.024.

[26] Q. Chen, Q. Liu, J. Hubert, W. Huang, K. Baert, G. Wallaert, H. Terryn, M.-P. Delplancke-Ogletree, F. Reniers, Deposition of photocatalytic anatase titanium dioxide films by atmospheric dielectric barrier discharge, Surf. Coat. Technol. 310 (2017) 173–179, https://doi.org/10.1016/j.surfcoat.2016.12.077.

[27] M. Hannula, H. Ali-Löytty, K. Lahtonen, E. Sarlin, J. Saari, M. Valden, Improved stability of atomic layer deposited amorphous TiO $_2$ Photoelectrode coatings by thermally induced oxygen defects, Chem. Mater. 30 (2018) 1199–1208, https://doi.org/10.1021/acs.chemmater.7b02938.

[28] S. Kang, R. Mauchauffé, Y.S. You, S.Y. Moon, Insights into the role of plasma in atmospheric pressure chemical vapor deposition of titanium dioxide thin films, Sci. Rep. 8 (2018) 16684, https://doi.org/10.1038/s41598-018-35154-4.

[29] L. Hoffmann, D. Theirich, S. Pack, F. Kocak, D. Schlamm, T. Hasselmann, H. Fahl, A. Räupke, H. Gargouri, T. Riedl, Gas diffusion barriers prepared by spatial atmospheric pressure plasma enhanced ALD, ACS Appl. Mater. Interfaces 9 (2017) 4171–4176, https://doi.org/10.1021/acsami.6b13380.

[30] C. Koral, M. Fantauzzi, C. Imparato, G.P. Papari, B. Silvestri, A. Aronne, A. Andreone, A. Rossi, Defects in the amorphous–crystalline evolution of gel-derived TiO_2, J. Phys. Chem. C 124 (2020) 23773–23783, https://doi.org/10.1021/acs.jpcc.0c07568.

[31] Z. He, W. Que, J. Chen, Y. He, G. Wang, Surface chemical analysis on the carbon-doped mesoporous TiO2 photocatalysts after post-thermal treatment: XPS and FTIR characterization, J. Phys. Chem. Solids 74 (2013) 924–928, https://doi.org/10.1016/j.jpcs.2013.02.001.

[32] Y. Gazal, C. Dublanche-Tixier, C. Chazelas, M. Colas, P. Carles, P. Tristant, Multi-structural TiO2 film synthesised by an atmospheric pressure plasma-enhanced chemical vapour deposition microwave torch, Thin Solid Films 600 (2016) 43–52, https://doi.org/10.1016/j.tsf.2016.01.011.

[33] N.D. Boscher, S. Olivier, R. Maurau, S. Bulou, T. Sindzingre, T. Belmonte, P. Choquet, Photocatalytic anatase titanium dioxide thin films deposition by an atmospheric pressure blown arc discharge, Appl. Surf. Sci. 311 (2014) 721–728, https://doi.org/10.1016/j.apsusc.2014.05.145.

[34] X. Jiang, Y. Zhang, J. Jiang, Y. Rong, Y. Wang, Y. Wu, C. Pan, Characterization of oxygen vacancy associates within hydrogenated TiO_2: a positron annihilation study, J. Phys. Chem. C 116 (2012) 22619–22624, https://doi.org/10.1021/jp307573c.

[35] H.H. Pham, L.-W. Wang, Oxygen vacancy and hole conduction in amorphous TiO $_2$, Phys. Chem. Chem. Phys. 17 (2015) 541–550, https://doi.org/10.1039/C4CP04209C.

[36] G.A. Tompsett, G.A. Bowmaker, R.P. Cooney, J.B. Metson, K.A. Rodgers, J. M. Seakins, The Raman spectrum of brookite, TiO2 (Pbca, Z = 8), J. Raman Spectrosc. 26 (1995) 57–62, https://doi.org/10.1002/jrs.1250260110.

[37] S. Kelly, F.H. Pollak, M. Tomkiewicz, Raman spectroscopy as a morphological probe for TiO_2 aerogels, J. Phys. Chem. B 101 (1997) 2730–2734, https://doi.org/10.1021/jp962747a.

[38] A. Pottier, S. Cassaignon, C. Chanéac, F. Villain, E. Tronc, J.-P. Jolivet, Size tailoring of TiO_2 anatase nanoparticles in aqueous medium and synthesis of nanocomposites. Characterization by Raman spectroscopy, J. Mater. Chem. 13 (2003) 877–882, https://doi.org/10.1039/b211271j.

[39] X. Xue, W. Ji, Z. Mao, H. Mao, Y. Wang, X. Wang, W. Ruan, B. Zhao, J.R. Lombardi, Raman investigation of nanosized TiO_2: effect of crystallite size and quantum confinement, J. Phys. Chem. C 116 (2012) 8792–8797, https://doi.org/10.1021/jp2122196.

[40] D. Georgescu, L. Baia, O. Ersen, M. Baia, S. Simon, Experimental assessment of the phonon confinement in TiO $_2$ anatase nanocrystallites by Raman spectroscopy: phonon confinement in TiO2 anatase nanocrystallites, J. Raman Spectrosc. 43 (2012) 876–883, https://doi.org/10.1002/jrs.3103.

[41] H. Yasuda, T. Hirotsu, Critical evaluation of conditions of plasma polymerization, J. Polym. Sci. Polym. Chem. Ed. 16 (1978) 743–759, https://doi.org/10.1002/pol.1978.170160403.

[42] A. Panepinto, D. Cossement, R. Snyders, Experimental and theoretical study of the synthesis of N-doped TiO2 by N ion implantation of TiO2 thin films, Appl. Surf. Sci. 541 (2021), 148493, https://doi.org/10.1016/j.apsusc.2020.148493.

[43] J.S. Dalton, P.A. Janes, N.G. Jones, J.A. Nicholson, K.R. Hallam, G.C. Allen, Photocatalytic oxidation of NOx gases using TiO_2: a surface spectroscopic approach, Environ. Pollut. 8 (2002).

[44] A. Panepinto, D. Cornil, P. Guttmann, C. Bittencourt, J. Cornil, R. Snyders, Fine control of the chemistry of nitrogen doping in TiO_2: a joint experimental and theoretical study, J. Phys. Chem. C 124 (2020) 17401–17412, https://doi.org/10.1021/acs.jpcc.0c05003.

[45] C. Bittencourt, M. Rutar, P. Umek, A. Mrzel, K. Vozel, D. Arčon, K. Henzler, P. Krüger, P. Guttmann, Molecular nitrogen in N-doped TiO $_2$ nanoribbons, RSC Adv. 5 (2015) 23350–23356, https://doi.org/10.1039/C4RA14410D.

[46] J. Szanyi, J.H. Kwak, S. Burton, J.A. Rodriguez, C.H.F. Peden, Characterization of NOx species in dehydrated and hydrated Na- and Ba-Y, FAU zeolites formed in NO2 adsorption, J. Electron Spectrosc. Relat. Phenom. 150 (2006) 164–170, https://doi.org/10.1016/j.elspec.2005.05.007.

[47] A.B. Preobrajenski, A.S. Vinogradov, S.L. Molodtsov, S.K. Krasnikov, T. Chassé, R. Szargan, C. Laubschat, Molecular effects in solid NaNO3 observed by x-ray absorption and resonant auger spectroscopy, Phys. Rev. B 65 (2002), 205116, https://doi.org/10.1103/PhysRevB.65.205116.

[48] V.N. Sivkov, A.S. Vinogradov, S.V. Nekipelov, D.V. Sivkov, D.V. Vyalykh, S. L. Molodtsov, Oscillator strengths for the shape resonances in the N K absorption spectrum of NaNO3 measured with the use of synchrotron radiation, Opt. Spectrosc. 101 (2006) 724–730, https://doi.org/10.1134/S0030400X06110117.

[49] G. Marcotte, P. Ayotte, A. Bendounan, F. Sirotti, C. Laffon, P. Parent, Dissociative adsorption of nitric acid at the surface of amorphous solid water revealed by X-ray absorption spectroscopy, J. Phys. Chem. Lett. 4 (2013) 2643–2648, https://doi.org/10.1021/jz401310j.

[50] Y. Chung, J.C. Lee, H.J. Shin, Direct observation of interstitial molecular N2 in Si oxynitrides, Appl. Phys. Lett. 86 (2005), 022901, https://doi.org/10.1063/1.1851620.

[51] J. Zhou, J. Wang, H. Liu, M.N. Banis, X. Sun, T.-K. Sham, Imaging nitrogen in individual carbon nanotubes, J. Phys. Chem. Lett. 1 (2010) 1709–1713, https://doi.org/10.1021/jz100376v.

[52] H. Chen, A. Nambu, J. Graciani Wen, J.C. Zhong, E. Hanson, J.A. Rodriguez Fujita, Reaction of NH $_3$ with Titania: N-doping of the oxide and TiN formation, J. Phys. Chem. C. 111 (2007) 1366–1372, https://doi.org/10.1021/jp066137e.

[53] A. Modi, N. Koratkar, E. Lass, B. Wei, P.M. Ajayan, Miniaturized Gas Ionization Sensors Using Carbon Nanotubes 424, 2003.
[54] J.Y. Kim, I. Kaganovich, H.-C. Lee, Review of the gas breakdown physics and nanomaterial-based ionization gas sensors and their applications, Plasma Sources Sci. Technol. 31 (2022), 033001, https://doi.org/10.1088/1361-6595/ac4574.
[55] P. Makuła, M. Pacia, W. Macyk, How to correctly determine the band gap energy of modified semiconductor photocatalysts based on UV–vis spectra, J. Phys. Chem. Lett. 9 (2018) 6814–6817, https://doi.org/10.1021/acs.jpclett.8b02892.
[56] S.K. Suram, P.F. Newhouse, J.M. Gregoire, High throughput light absorber discovery, part 1: an algorithm for automated Tauc analysis, ACS Comb. Sci. 18 (2016) 673–681, https://doi.org/10.1021/acscombsci.6b00053.
[57] R. Asahi, T. Morikawa, T. Ohwaki, K. Aoki, Y. Taga, Visible-light photocatalysis in nitrogen-doped titanium oxides, Science. 293 (2001) 269–271, https://doi.org/10.1126/science.1061051.
[58] M. Harb, P. Sautet, P. Raybaud, Origin of the enhanced visible-light absorption in N-doped bulk anatase TiO_2 from first-principles calculations, J. Phys. Chem. C 115 (2011) 19394–19404, https://doi.org/10.1021/jp204059q.
[59] N. Umezawa, J. Ye, Role of complex defects in photocatalytic activities of nitrogen-doped anatase TiO2, Phys. Chem. Chem. Phys. 14 (2012) 5924, https://doi.org/10.1039/c2cp24010f.
[60] K. Zhang, L. Yin, G. Liu, H.-M. Cheng, Accurate structural descriptor enabled screening for nitrogen and oxygen vacancy codoped TiO2 with a large bandgap narrowing, J. Mater. Sci. Technol. 122 (2022) 84–90, https://doi.org/10.1016/j.jmst.2021.12.062.
[61] K. Komaguchi, T. Maruoka, H. Nakano, I. Imae, Y. Ooyama, Y. Harima, Electron-transfer reaction of oxygen species on TiO_2 nanoparticles induced by sub-band-gap illumination, J. Phys. Chem. C 114 (2010) 1240–1245, https://doi.org/10.1021/jp909678e.
[62] T. Cottineau, A. Rouet, V. Fernandez, L. Brohan, M. Richard-Plouet, Intermediate band in the gap of photosensitive hybrid gel based on titanium oxide: role of coordinated ligands during photoreduction, J. Mater. Chem. A 2 (2014) 11499–11508, https://doi.org/10.1039/C4TA02127D.